



# Non-linear 3-D semi-analytical model for an axial flux reluctance magnetic coupling

Rémi Dorget, Thierry Lubin

## ► To cite this version:

Rémi Dorget, Thierry Lubin. Non-linear 3-D semi-analytical model for an axial flux reluctance magnetic coupling. IEEE Transactions on Energy Conversion, 2022, pp.1-1. 10.1109/TEC.2022.3153173 . hal-03586935

**HAL Id: hal-03586935**

**<https://hal.science/hal-03586935>**

Submitted on 24 Feb 2022

**HAL** is a multi-disciplinary open access archive for the deposit and dissemination of scientific research documents, whether they are published or not. The documents may come from teaching and research institutions in France or abroad, or from public or private research centers.

L'archive ouverte pluridisciplinaire **HAL**, est destinée au dépôt et à la diffusion de documents scientifiques de niveau recherche, publiés ou non, émanant des établissements d'enseignement et de recherche français ou étrangers, des laboratoires publics ou privés.

# Non-linear 3-D semi-analytical model for an axial-flux reluctance magnetic coupling

Rémi Dorget and Thierry Lubin

**Abstract**—This article presents a 3-D semi-analytical model of an axial-flux reluctance coupling. Thanks to the separation of variables method, Fourier series analysis and the convolution theorem (i.e. Cauchy's product), the salient-pole region is modelled by a spatially variable magnetic permeability. Additionally, an iterative algorithm is implemented to account for the magnetic saturation of the iron teeth. The results of the proposed model are compared with a previously published 2-D semi-analytical model, 3-D finite-element method and experimental results. The proposed method appears to be an appropriate tool for the design process of reluctance couplings in cases where the salient poles are saturated.

**Index Terms**—Magnetic coupling, variable reluctance, three-dimensional analytical model, magnetic saturation.

## I. INTRODUCTION

MAGNETIC couplings are electromagnetic devices used to transmit rotational movement between two shafts without mechanical contact. They can be typically employed in applications which need to transmit a torque through a sealed wall [1]. Additionally, they provide a natural resilience against overloads.

Magnetic couplings consist of two rotors with an identical number of pole pairs. There are two types of magnetic couplings. Synchronous magnetic couplings in which both rotors rotate at the same speed [2] and asynchronous magnetic couplings in which the torque transmission is due to induced currents and the transmittable torque depends on the slip between the two rotors [3]. Both types of magnetic couplings can be found in radial-flux or axial-flux form [4], [5].

Among the synchronous couplings, the most widespread technology is the permanent magnets (PM) couplings composed of two similar PM rotors facing each other. This topology provides the highest pull-out torque density [6] but is the most expensive as rare-earth materials are required for both rotors. Reluctance couplings are a less common topology of synchronous couplings [7]. As shown on Fig. 1 a), they also comprise two rotors, one with PM and a second one with soft-steel salient poles (SP). Therefore, reluctance couplings require less rare-earth material than their PM counterparts and are consequently cheaper. Moreover, the absence of PM on one rotor allows it to be used in harsher environments such as at

high temperatures. However, these gains are achieved at the expense of the torque density.

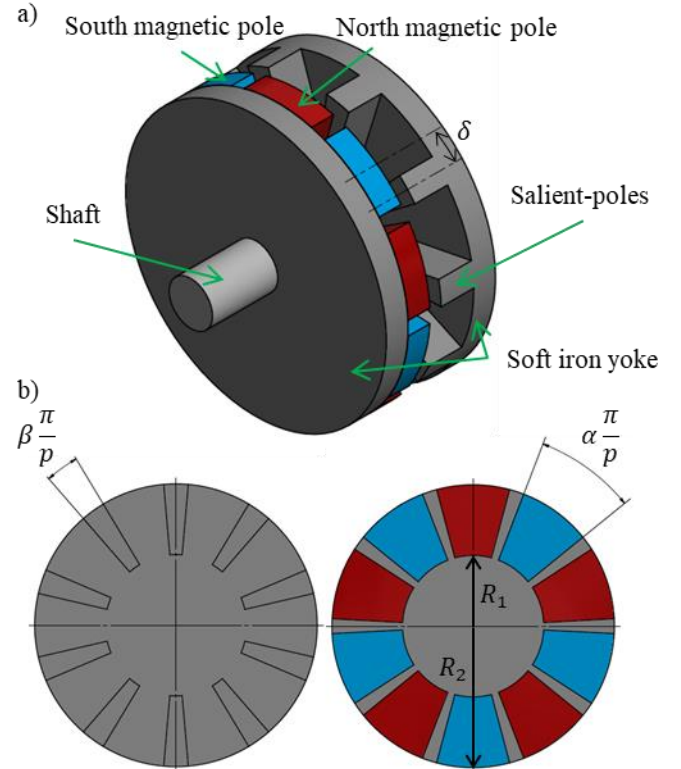


Fig. 1. Component and geometrical parameters of a reluctance magnetic coupling. a) 3-D representation. b) Cross sectional views in the  $(r, \theta)$  plane.

The design of magnetic devices such as magnetic couplings requires fast and precise modelling tools for optimization processes. The finite-element method (FEM) is an accurate and easy to implement option but requires an important computation time especially in 3-D. Therefore, analytical and semi-analytical methods using separation of variables, Fourier series analysis and separation of space in subdomain in which the Maxwell's equations are solved are often preferred for their lower computational cost. In previous works, 3-D analytical models for axial-flux magnetic couplings have been proposed for both PM couplings [8] and asynchronous couplings [9], [10]. More recently, a 2-D semi-analytical model of a reluctance coupling has been developed from a simplified geometry by neglecting the curvature and considering the end

Rémi Dorget is with Université de Lorraine, GREEN, F-54000 Nancy, France and also with Safran Tech, Electrical & Electronic Systems Research group, Rue des Jeunes Bois, Châteaufort, 78114 Magny-Les-Hameaux, France (e-mail: remi.dorget@safrangroup.com).

Thierry Lubin is with Université de Lorraine, GREEN, F-54000 Nancy, France (e-mail: thierry.lubin@univ-lorraine.fr).

effects in the torque and axial force calculation by using a correction factor [11]. The proposed model proved to be accurate for wide air-gaps at a very small computational cost. Nevertheless, for small air-gaps and more generally for arrangements where the SP of the reluctant rotor are highly saturated, the model was not able to determine the pull-out torque precisely. Indeed, an important assumption was that the iron of the SP had an infinite magnetic permeability which allowed to model the SP as a simple boundary condition. Consequently, the model was able to predict the optimal SP opening for a 3 mm air-gap but not for a 1 mm air-gap [11]. These results have shown the necessity of accounting the iron saturation in the analytical modelling of reluctance actuators.

The method proposed in [11] could be improved by modelling the SP as a subdomain with a finite permeability using the superposition technique described in [12], [13]. With this technique, an iterative process can be implemented to account for the global saturation of the SP. However, it requires solving Maxwell's equations in an additional subdomain with different eigenvalues, and then increase the computational time.

Lately, several research groups developed 2-D cylindrical semi-analytical models of radial-flux actuators including subdomains with a spatially variable permeability allowing notably to affect a finite value to the SP permeability without increasing the number of subdomains [14]–[16] and also to implement global saturation iterative algorithms [17], [18]. The method employed is based on the convolution theorem (i.e. Cauchy's product) which allows to consider complex space distribution of the magnetic permeability. In a recent article, we improved the method by applying it to an axial-flux superconducting flux modulation machine [19]. The proposed 3-D model was a cartesian model considering subdomains with a permeability variable in two directions allowing to approach the magnetic behavior of superconducting bulks. The use of the Cauchy product allows, especially in 3D, to reduce the number of sub-domains compared to the superposition technique. Moreover, it should be noted that the superposition technique is complex to implement on geometries with several magnetic saliencies because the number of subdomains can become very high. For instance, the 2-D model geometry of [20] is divided in 23 subdomains.

In this article, we apply the method presented in [19] to propose a new 3-D semi-analytical model of the axial-flux reluctance coupling of Fig. 1. Thanks to the convolution theorem, the model considers the non-linear magnetic behavior and the end effects of the iron SP while using only few subdomains. The results provided by the model are compared with [11], 3-D non-linear FEM and experimental tests.

## II. SEMI-ANALYTICAL MODEL

### A. Geometrical parameters

Fig.1 shows the actual geometry of the reluctance couplings with the following geometrical parameters.  $R_1$  is the inner radius of the PM and SP,  $R_2$  is the outer radius,  $p$  is the number of pole pairs,  $\alpha$  is the PM opening,  $\beta$  is the SP opening,  $\delta$  is the torque angle i.e. the shift angle between the PM center and the

SP center,  $W_a$  is the magnet thickness,  $W_b$  is the air-gap length and  $W_c$  is the SP thickness, as shown in Fig. 2.

### B. Consideration of the radial end effects

In [11], a 2-D simple model defined at the mean radius has been developed assuming that the magnetic field is invariant along the radial direction and equal to the value at the mean radius. With this assumption both the so-called end and curvature effects were neglected. However, as will be shown later in the article (Fig. 15), the magnetic field drops down rapidly near the top and bottom edges of the PM because of the end effects clearly showing a limit of the 2-D model. Thus, we must propose a 3-D model in order to account for the variation of the magnetic field along the radial direction.

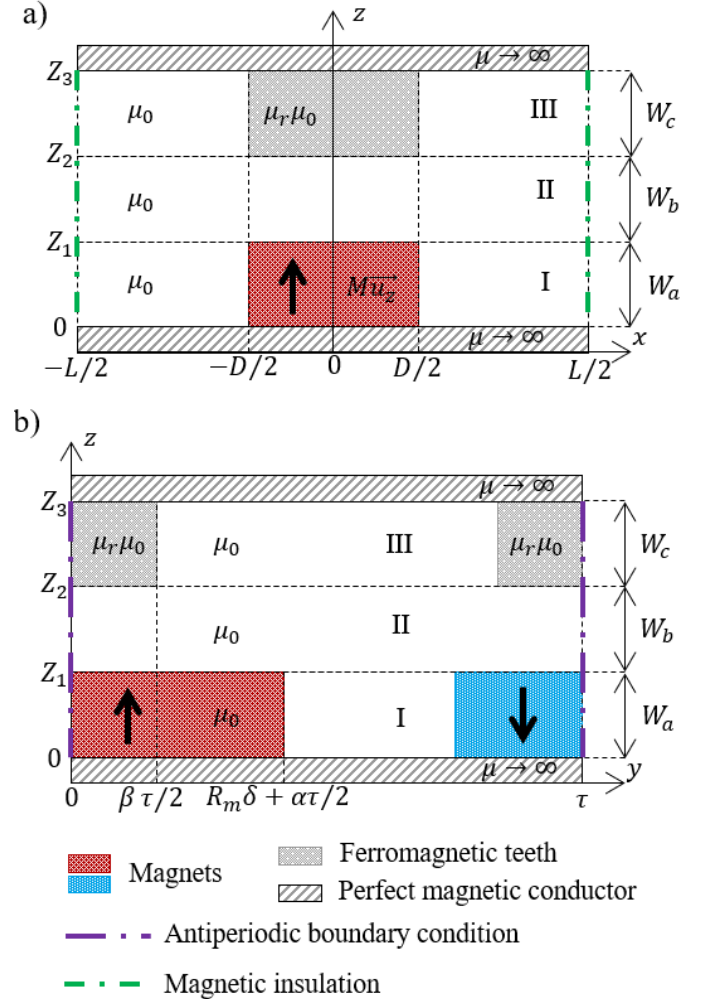


Fig. 2. Sectional view of the cartesian problem with the different domains and parameters of the problem. a) (xz) plane b) (yz) plane

In order to simplify the geometry, the curvature effects are neglected by linearizing to the mean radius  $R_m = (R_2 + R_1)/2$ . Hence, the problem can be solved in Cartesian coordinates with the x-axis representing the radial direction and the y-axis representing the azimuthal direction. The x-coordinate is related to the r coordinate by  $x = r - R_m$  whereas the y-coordinate is related to the  $\theta$ -coordinate by  $y = R_m \theta$ . Thus, the cross-sectional views of the Cartesian problem are shown in Fig. 2 a) and b) for the (xz) and (yz) planes respectively. As

shown on Fig. 2 a) the variation in the radial direction is considered to model the end effects since the PM and SP height is finite. Moreover, in the radial direction, we must define two artificial external boundary conditions to limit the geometry. These boundaries must be located far enough away from the PM and SP so as not to affect the result.

Finally, one can note that, in the Cartesian frame, the height of the PM and SP is  $D = R_2 - R_1$ , a pole width is  $\tau = R_m \pi / p$ , the PM width is  $\alpha \tau / 2$  and the SP width is  $\beta \tau / 2$ . The linearization to the mean radius is a common method to simplify the modelling of axial-flux actuator and has been successfully applied for various topologies in previous works [8], [9] [19].

### C. Boundary conditions and Fourier series representation

From this section, the superscripts of the magnetic quantities will denote the index of the subdomains and the subscripts will correspond to the harmonic ranks and the directions of the vector components. Finally, the terms in bold correspond to matrix and vector terms.

As shown in Fig. 2, the geometry is divided in 3 subdomains, the PM region with a spatially variable magnetization (region I), the air-gap (region II) and the SP region (region III) with a spatially variable permeability. As there is no current in any of the subdomains, the magnetic field  $\vec{H}^i$  in region  $i$  will be expressed as a magnetic scalar potential  $\Phi^i$  defined as:

$$\vec{H}^i = -\nabla \Phi^i \quad (i = I, II, III) \quad (1)$$

In the z-direction, the geometry is limited by the soft iron yokes whose permeability is supposed to be infinite leading to the orthogonality of the flux density at the yoke surface. Expressed in magnetic scalar potential, the boundary conditions in  $z = 0$  and  $z = Z_3 = W_a + W_b + W_c$  are:

$$\Phi^I(x, y, 0) = \Phi^{III}(x, y, Z_3) = 0 \quad (2)$$

The PM periodicity leads to a system of odd boundary conditions in the y-direction:

$$\Phi^i(x, 0, z) = -\Phi^i(x, \tau, z) \quad (3)$$

In the x-direction, the external limits of the problem are located at  $x = L/2$  and  $x = -L/2$  at which the boundary condition is a magnetic insulation leading to the following Neumann condition on the scalar potential:

$$\frac{\partial \Phi^i}{\partial x} \left( \frac{L}{2}, y, z \right) = \frac{\partial \Phi^i}{\partial x} \left( -\frac{L}{2}, y, z \right) = 0 \quad (4)$$

The limit in the x-direction is fixed at  $L = 3D$ , this value is defined from our experience of previous models [19].

Additionally, at the boundaries between the regions in  $z = Z_1 = W_a$  and  $z = Z_2 = W_a + W_b$ , the interface conditions ensure the continuity of the flux density orthogonal component and the magnetic field tangential components.

According to the conditions (3) and (4) and by applying the separation of variables, the magnetic scalar potential in each domain can be expressed in terms of complex Fourier series:

$$\Phi^i(x, y, z) = \sum_{n=-N}^{+N} \sum_{k=-N}^{+N} \hat{\Phi}_{n,k}^i(z) e^{j \frac{2n\pi}{L} x} e^{j \frac{k\pi}{\tau} y} \quad (5)$$

The eigenvalues in the x and y directions are  $2\pi n/L$  and  $k\pi/\tau$  respectively, with  $n$  and  $k$  denote the harmonic ranks.  $N$  represent the highest spatial harmonic considered. We chose

an identical number of harmonics in both directions for the sake of simplicity. The impact of  $N$  on the computation time and accuracy of the model will be discussed below. Similarly, the component  $u$  ( $u = x, y, z$ ) in domain  $i$  of the magnetic field  $H_u^i$  and the flux density  $B_u^i$  can be expressed as:

$$H_u^i(x, y, z) = \sum_{n=-N}^{+N} \sum_{k=-N}^{+N} \hat{H}_{u,n,k}^i(z) e^{j \frac{2n\pi}{L} x} e^{j \frac{k\pi}{\tau} y} \quad (6)$$

$$B_u^i(x, y, z) = \sum_{n=-N}^{+N} \sum_{k=-N}^{+N} \hat{B}_{u,n,k}^i(z) e^{j \frac{2n\pi}{L} x} e^{j \frac{k\pi}{\tau} y} \quad (7)$$

As a result of this representation, only the z-dependent coefficients of the scalar potential  $\hat{\Phi}_{n,k}^i(z)$ , the magnetic field  $\hat{H}_{u,n,k}^i(z)$  and the flux density  $\hat{B}_{u,n,k}^i(z)$ , are still to be determined.

Additionally, in order to solve the problem, the magnetization in region I and the magnetic permeability in region III must be expressed in Fourier series as well:

$$\vec{M}^I = M^I(x, y) \vec{u}_z = \sum_{n=-N}^{+N} \sum_{k=-N}^{+N} \hat{M}_{n,k}^I e^{j \frac{2n\pi}{L} x} e^{j \frac{k\pi}{\tau} y} \quad (8)$$

$$\mu^{III}(x, y) = \sum_{n=-\infty}^{+\infty} \sum_{k=-\infty}^{+\infty} \hat{\mu}_{n,k}^{III} e^{j \frac{2n\pi}{L} x} e^{j \frac{k\pi}{\tau} y} \quad (9)$$

Where the coefficients  $\hat{M}_{n,k}^I$  are:

$$\hat{M}_{n,k}^I = \begin{cases} 0 & \text{for } k \text{ even,} \\ \frac{2B_{rem}D}{\mu_0 \pi k L} \sin\left(\frac{k\pi\alpha}{2}\right) e^{-jk\pi \frac{R_m \delta}{\tau}} & \text{for } n = 0 \text{ and } k \text{ odd } \neq 0, \\ \frac{2B_{rem}}{\mu_0 \pi^2 n k} \sin\left(\frac{n\pi D}{L}\right) \sin\left(\frac{k\pi\alpha}{2}\right) e^{-jk\pi \frac{R_m \delta}{\tau}} & \text{for } n \neq 0 \text{ and } k \text{ odd } \neq 0 \end{cases} \quad (10)$$

Where  $B_{rem}$  is the remanant flux density of the PM. It should be noted that we assume the magnets to have a relative permeability equal to 1. The coefficients  $\hat{\mu}_{n,k}^{III}$  are:

$$\hat{\mu}_{n,k}^{III} = \begin{cases} 0 & \text{for } k \text{ odd,} \\ \mu_0 \left(1 + (\mu_r - 1) \beta \frac{D}{L}\right) & \text{for } n = 0 \text{ and } k = 0, \\ \frac{\mu_0 \beta}{n\pi} (\mu_r - 1) \sin\left(\frac{n\pi D}{L}\right) & \text{for } n \neq 0 \text{ and } k = 0, \\ \frac{2\mu_0 D}{k\pi L} (\mu_r - 1) \sin\left(\frac{k\pi\beta}{2}\right) & \text{for } n = 0 \text{ and } k \neq 0, \\ \frac{2\mu_0}{k n \pi^2} (\mu_r - 1) \sin\left(\frac{k\pi\beta}{2}\right) \sin\left(\frac{n\pi D}{L}\right) & \text{for } n \neq 0 \text{ and } k \neq 0 \end{cases} \quad (11)$$

### D. Convolution theorem and matrix form

The constitutive relation between  $B_u^{III}$  and  $H_u^{III}$  in region III is:

$$B_u^{III}(x, y, z) = \mu^{III}(x, y) H_u^{III}(x, y, z) \quad (12)$$

Using the Cauchy's product, (12) can be rewritten in terms of Fourier series coefficients [19]:

$$\hat{B}_{u,n,k}^{III}(z) = \sum_{n'=-N}^{+N} \sum_{k'=-N}^{+N} \hat{\mu}_{n-n',k-k'}^{III} \hat{H}_{u,n',k'}^{III}(z) \quad (13)$$

Equation (13) shows that in region III, each harmonic of  $B_u^{III}$  depends on all harmonics of  $H_u^{III}$  which will lead to a system of differential equations that must be solved in matrix form. Thus, (13) is rewritten for each component as follows:

$$\mathbf{B}_x^{III} = \boldsymbol{\mu}_{c,x}^{III} \mathbf{H}_x^{III} \quad (14)$$

$$\mathbf{B}_y^{III} = \boldsymbol{\mu}_{c,y}^{III} \mathbf{H}_y^{III} \quad (15)$$

$$\mathbf{B}_z^{III} = \boldsymbol{\mu}_{c,z}^{III} \mathbf{H}_z^{III} \quad (16)$$

Here,  $\mathbf{B}_u^I$  denotes the column vector gathering the Fourier series coefficients  $\hat{B}_{x,n,k}^{III}$ . We can similarly define  $\mathbf{H}_u^I$ ,  $\Phi^I$  and  $\mathbf{M}_u^I$  for the magnetic field, the scalar potential and magnetization in each region, the vector concatenation structure in 3-D is presented in [19]. Moreover,  $\boldsymbol{\mu}_{c,x}^{III}$ ,  $\boldsymbol{\mu}_{c,y}^{III}$  and  $\boldsymbol{\mu}_{c,z}^{III}$  denotes the permeability convolution matrices for the different components of the constitutive relation whose concatenation structure is also presented in [19].

Several points are to be noted here. Firstly, it can be seen from (10) that the  $k$  even coefficients of  $\hat{M}_{n,k}^I$  are equal to zero whereas the  $k$  odd coefficients of  $\hat{\mu}_{n,k}^{III}$  are null. The vector and matrix form of each Fourier series must also include the zero coefficients to ensure the correspondence between each harmonic.

Secondly, care should be taken while calculating the convolution matrices coefficients to avoid convergence problem [14]. Indeed, at the boundaries between tooth and air in region III, the perpendicular component of  $\vec{B}$  and the tangential component of  $\vec{H}$  are continuous whereas the perpendicular component of  $\vec{H}$  and the tangential component of  $\vec{B}$  are discontinuous. For instance, on the (xz) boundary of the SP, both the right and left-hand side of (14) contain a single discontinuous parameter which does not cause any convergence issues. However, in (15), the right-hand side is continuous whereas the left-hand side is the product of two discontinuous terms which leads to convergence issues. As described in [21], this can be solved by defining to kinds of convolution matrices,  $\boldsymbol{\mu}_c^{III}$  and  $(1/\boldsymbol{\mu}_c)^{III}$ . On one hand, the matrix  $\boldsymbol{\mu}_c^{III}$  is the most obvious and defined by the concatenation of the coefficients  $\hat{\mu}_{n,k}^{III}$  from (11). On the other hand,  $(1/\boldsymbol{\mu}_c)^{III}$  is defined as the concatenation of the Fourier series coefficients of  $1/\mu^{III}(x,y)$  which can be calculated by replacing  $\mu_0$  and  $\mu_r$  by  $1/\mu_0$  and  $1/\mu_r$  in (11). Doing so, there is two ways to express the constitutive relation:

$$\mathbf{B}_u^{III} = \boldsymbol{\mu}_c^{III} \mathbf{H}_u^{III} \quad (17)$$

And

$$\mathbf{H}_u^{III} = (1/\boldsymbol{\mu}_c)^{III} \mathbf{B}_u^{III} \quad (18)$$

Thus, expressing (14) using (17) and (15) using (18) will ensure the convergence on the (xz) boundary of the SP. This method is well known in 2-D, but in 3-D an additional problem arises. Indeed, it is not possible to ensure a perfect convergence of every component on each SP boundary in region III. Still using the example of (14), on the (yz) boundary,  $B_y^{III}$  is the

discontinuous field whereas  $H_y^{III}$  is continuous. Therefore, using (18) will lead to a bad convergence of this component [21]. Consequently, the convergence of certain components must be sacrificed on certain faces of the SP. Nonetheless, since the boundary condition between air and iron leads the tangential components to be significantly smaller than the perpendicular components, the most appropriate option here is to arrange (14-16) to ensure a good convergence of the perpendicular components. Therefore, (14) and (15) are expressed using (17) whereas (16) is expressed using (18) leading to:

$$\boldsymbol{\mu}_{c,x}^{III} = ((1/\boldsymbol{\mu}_c)^{III})^{-1} \quad (19)$$

$$\boldsymbol{\mu}_{c,y}^{III} = ((1/\boldsymbol{\mu}_c)^{III})^{-1} \quad (20)$$

$$\boldsymbol{\mu}_{c,z}^{III} = \boldsymbol{\mu}_c^{III} \quad (21)$$

Lastly, it should be noted that the constitutive relations in regions I and II should also be expressed in matrix form. Since the permeability is uniform in these domains, the matrices  $\boldsymbol{\mu}_c^I$ ,  $\boldsymbol{\mu}_c^{II}$ ,  $(1/\boldsymbol{\mu}_c)^I$  and  $(1/\boldsymbol{\mu}_c)^{II}$  are diagonal and equal to:

$$\boldsymbol{\mu}_c^I = ((1/\boldsymbol{\mu}_c)^I)^{-1} = \mu_0 \mathbf{I}_{(2N+1)^2} \quad (i = I \text{ or } II) \quad (22)$$

Where  $\mathbf{I}_{(2N+1)^2}$  is the identity matrix.

#### E. Magnetostatic field solution

Using the matrix form described above, the relation (1) becomes:

$$\mathbf{H}_x^I = -j \frac{2\pi}{L} \mathbf{N}_x \Phi^I \quad (23)$$

$$\mathbf{H}_y^I = -j \frac{\pi}{\tau} \mathbf{N}_y \Phi^I \quad (24)$$

$$\mathbf{H}_z^I = -\frac{\partial}{\partial z} \Phi^I \quad (25)$$

Where the matrix  $\mathbf{N}_x$  and  $\mathbf{N}_y$  are diagonal matrices of indexes  $n$  and  $k$  whose structure is described in [19]. In scalar potential, the partial differential equation is derived from the Gauss law for magnetism:

$$\nabla \cdot \vec{B}^I = 0 \quad (26)$$

Since the divergence of the magnetization in region I is equal to zero, the magnetostatic equation to solve in each domain is derived from (1), (14), (15), (16) and (26):

$$\frac{\partial^2}{\partial z^2} \Phi^I - \mathbf{V}^{I^2} \Phi^I = 0 \quad (27)$$

Where in regions I and II:

$$\mathbf{V}^I = \mathbf{V}^{II} = \left( \left( \frac{2\pi}{L} \right)^2 \mathbf{N}_x^2 + \left( \frac{\pi}{\tau} \right)^2 \mathbf{N}_y^2 \right)^{\frac{1}{2}} \quad (28)$$

And in the region III:

$$\mathbf{V}^{III} = \left( \left( \frac{2\pi}{L} \right)^2 \boldsymbol{\mu}_{c,z}^{III^{-1}} \mathbf{N}_x \boldsymbol{\mu}_{c,x}^{III} \mathbf{N}_x + \left( \frac{\pi}{\tau} \right)^2 \boldsymbol{\mu}_{c,z}^{III^{-1}} \mathbf{N}_y \boldsymbol{\mu}_{c,y}^{III} \mathbf{N}_y \right)^{\frac{1}{2}}$$

In order to solve (27), eigen decomposition must be applied to  $\mathbf{V}^{III}$ :

$$\mathbf{V}^{III} = \mathbf{P}^{III} \mathbf{D}^{III} \mathbf{P}^{III^{-1}} \quad (29)$$

Where  $\mathbf{P}^{III}$  and  $\mathbf{D}^{III}$  are the eigenvector matrix and eigenvalue matrix of  $\mathbf{V}^{III}$ .

According to the boundary conditions, the solutions of (27) are, in region I:

$$\Phi^I = \frac{\sinh(\mathbf{V}^I z)}{\sinh(\mathbf{V}^I Z_1)} \mathbf{a} \quad (30)$$

In region II:

$$\Phi^{II} = \frac{\sinh(\mathbf{V}^{II}(z - Z_2))}{\sinh(\mathbf{V}^{II}(Z_1 - Z_2))} \mathbf{a} + \frac{\sinh(\mathbf{V}^{II}(z - Z_1))}{\sinh(\mathbf{V}^{II}(Z_2 - Z_1))} \mathbf{b} \quad (31)$$

And in region III:

$$\Phi^{III} = \mathbf{P}^{III} \frac{\sinh(\mathbf{D}^{III}(z - Z_3))}{\sinh(\mathbf{D}^{III}(Z_2 - Z_3))} \mathbf{P}^{III-1} \mathbf{b} \quad (32)$$

Where the hyperbolic functions of matrix inputs are defined similarly to hyperbolic functions for scalar inputs.  $\mathbf{a}$  and  $\mathbf{b}$  are column vectors containing the unknown coefficients which are calculated using the following interface conditions:

$$\frac{\partial}{\partial z} \Phi^I - \frac{\partial}{\partial z} \Phi^{II} \Big|_{z=Z_1} = \mathbf{M}^I \quad (33)$$

$$\mu_0 \frac{\partial}{\partial z} \Phi^{II} \Big|_{z=Z_2} = \mu_c^{III} \frac{\partial}{\partial z} \Phi^{III} \Big|_{z=Z_2} \quad (34)$$

The system of linear equations (33-34) is to be solved numerically to determine  $\mathbf{a}$  and  $\mathbf{b}$  [14], [19].

#### F. Calculation of the torque and axial force

The electromagnetic torque  $T_z$  and axial force  $F_z$  are determined from the Maxwell stress tensor. The integration surface is the boundary between regions I and II:

$$T_z = p \mu_0 R_m \int_{-\frac{L}{2}}^{\frac{L}{2}} \int_0^{2\pi} H_z^{II}(x, y, Z_1) H_y^{II}(x, y, Z_1) dx dy \quad (35)$$

$$F_z = \frac{\mu_0 p}{2} \int_{-\frac{L}{2}}^{\frac{L}{2}} \int_0^{2\pi} (H_z^{II}(x, y, Z_1)^2 - H_x^{II}(x, y, Z_1)^2 - H_y^{II}(x, y, Z_1)^2) dx dy \quad (36)$$

Using (23-26) to derive the Fourier series coefficients of the magnetic field from the scalar potential, the torque can finally be expressed as:

$$T_z = 2p \mu_0 \tau L R_m \sum_{n=-\infty}^{+\infty} \sum_{k=-\infty}^{+\infty} \widehat{H}_y^{II}{}_{n,k}(Z_1) \widehat{H}_z^{II}{}_{-n,-k}(Z_1) \quad (37)$$

And the axial force can be expressed as:

$$F_z = p \mu_0 \tau L \sum_{n=-\infty}^{+\infty} \sum_{k=-\infty}^{+\infty} (\widehat{H}_z^{II}{}_{n,k}(Z_1) \widehat{H}_z^{II}{}_{-n,-k}(Z_1) - \widehat{H}_x^{II}{}_{n,k}(Z_1) \widehat{H}_x^{II}{}_{-n,-k}(Z_1) - \widehat{H}_y^{II}{}_{n,k}(Z_1) \widehat{H}_y^{II}{}_{-n,-k}(Z_1)) \quad (38)$$

#### G. Consideration of SP saturation

The model proposed above allows to consider a finite value for the average SP magnetic permeability  $\mu_r$ . Therefore, it is possible to implement an iterative method to account for the saturation of the SP. Each step of the iterative algorithm consists of calculating the average flux density in the SP base (between  $\frac{Z_2+Z_3}{2}$  and  $Z_3$ ) to calculate the permeability from the  $\mu_r - B$  curve shown on Fig. 3b and to update the  $\mu_r$  for the next iteration of the algorithm. The detailed algorithm used can be found in [18].

The iterative method requires to run the model and calculate the coefficients  $\mathbf{a}$  and  $\mathbf{b}$  several times. Usually, less than 20 steps are required to reach a permeability error inferior to 5 %.

It should be noted that the permeability is defined here as the ratio between the flux density and the magnetic field and not as the derivative of the flux density with respect to the magnetic field. Indeed, the iterative method simulate the non-linearities by a linear model with the same working point as the real system. Hence, Fig. 3a also presents the  $B - H$  curve from which the  $\mu_r - B$  curve is derived, as shown in Fig. 3b.

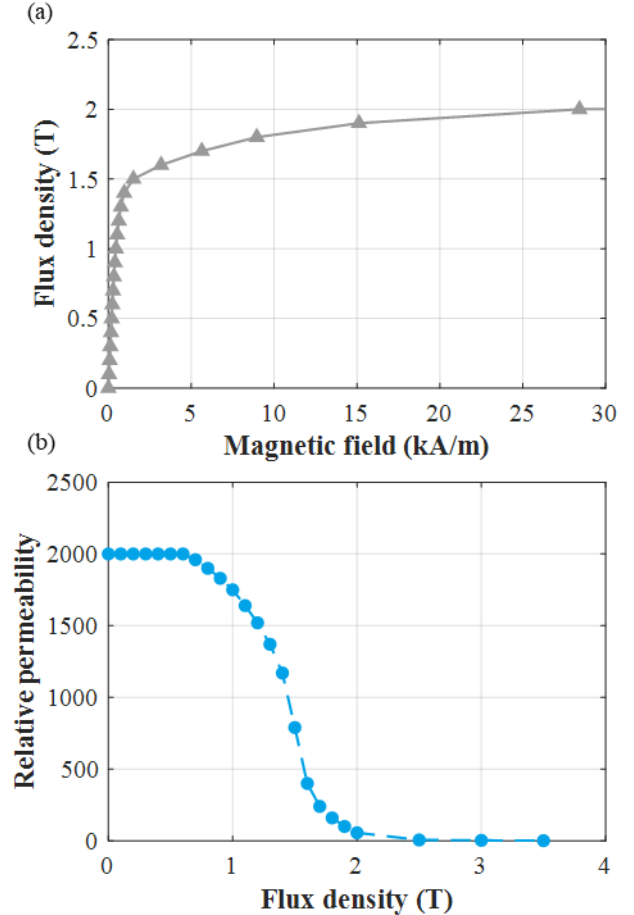


Fig. 3. Simplified  $B - H$  curve (a) of the low carbon steel (AISI-1010) used in the reluctance coupling's SP and corresponding  $\mu_r - B$  curve (b).



### III. COMPARISON WITH 3-D FEM

In this section, the accuracy and performances of the proposed model will be assessed by comparing the following models:

- The non-linear 3-D semi-analytical model (3D-SAM) proposed in section II with  $N = 10$  harmonics. As presented above this model considers the end effect of the SP but not the curvature effects using the linearization to the average radius. Additionally, the global saturation of the SP is accounted thanks to the iterative process.
- The 2-D semi-analytical model (2D-SAM) presented in [11] with  $N = 100$  harmonics. This model neglects the curvature effects and partially considers the end effects through a correction factor. The saturation is neglected as the SP permeability is supposed to be infinite.
- A non-linear 3-D FEM (3D-FEM) model considering the actual cylindrical geometry of Fig. 1 simulated on the software COMSOL with a scalar potential formulation. The mesh and an example of the flux density distribution is provided in [11]. The local iron saturation of the SP and back iron is considered in this model using the  $B - H$  curve of Fig. 3a. This model will be used as reference as it requires less assumptions

Table I presents the input parameters of the three models and the corresponding values for the studied coupling. These parameters correspond to the prototype used for the experimental measurement presented in the next section.

TABLE I

Parameters of the magnetic coupling		
Parameter	Description	Value
$R_1$	PM and SP inner radius	30 mm
$R_2$	PM and SP outer radius	60 mm
$W_a$	PM thickness	10 mm
$W_b$	Air-gap length	-
$W_c$	SP thickness	15 mm
$p$	Number of pole pairs	5
$\alpha$	PM to pole opening ratio	0.83
$\beta$	SP to pole opening ratio	0.23
$B_{rem}$	Remanent magnetization of the PM	1.25 T

#### A. Flux density distribution in the air-gap

Fig. 4 and Fig. 5 shows the axial and tangential components of the flux density distribution along the  $\theta$ -direction in the middle of the air-gap, at the average radius under no-load condition ( $\delta = 0$ ) for the three studied models. The air-gap length is fixed at  $W_b = 1$  mm. It can be observed that the three models have a similar behavior. However, on Fig. 4, one can note that the 3D-SAM gives a more precise value of the field amplitude than the 2D-SAM but has more ripples. Indeed, employing a 3-D model does not allow to select a large number of harmonics because two directions needs to be considered. Meanwhile, the 2D-SAM can use a substantial number of harmonics and present a smooth curve but does not account for the saturation leading to an error on the amplitude.

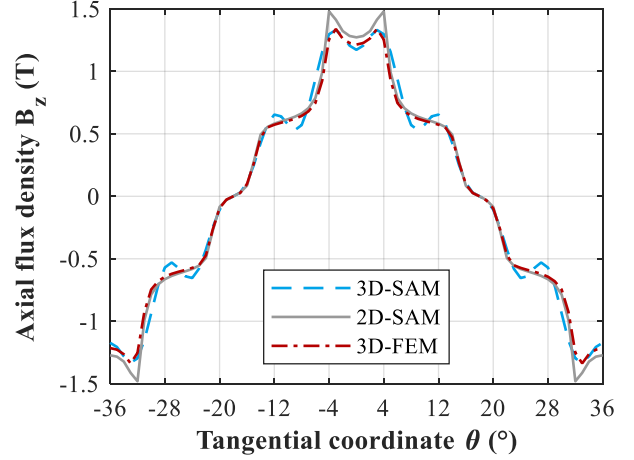


Fig. 4. Axial component of the flux density at the average radius, in the middle of the air-gap under no-load condition ( $W_b = 1$  mm,  $r = R_m$ ,  $z = W_a + W_b/2$  and  $\delta = 0$ ).

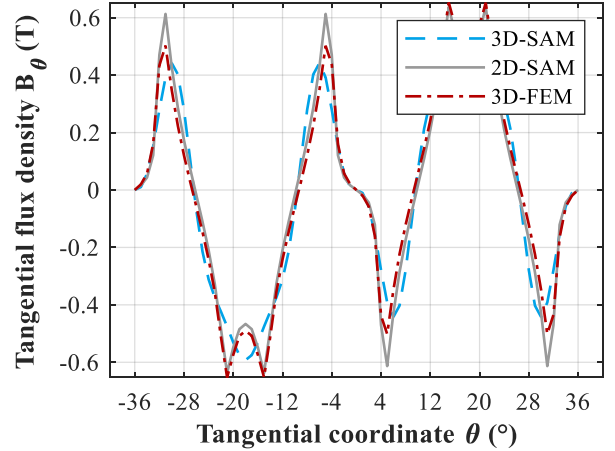


Fig. 5. Tangential component of the flux density at the average radius, in the middle of the air-gap under no-load condition ( $W_b = 1$  mm,  $r = R_m$ ,  $z = W_a + W_b/2$  and  $\delta = 0$ ).

In Fig. 5, similar conclusions can be drawn, except that the error made by the 3D-SAM seems to be larger as it cannot predict with so few harmonics the two peaks between  $22^\circ$  and  $12^\circ$ .

Fig. 6 and 7 shows the axial component of the flux density in the middle of the air-gap at the outer and inner radii, respectively. In both cases, we plotted the 2D-SAM but one should keep in mind that the 2D-SAM accounts for the end-effects only for the torque calculations which means that the distribution provided by 2D-SAM are identical for all radii. Therefore, the interest of using the 3D-SAM appears more clearly on these graphs as the end-effects are not negligible anymore on the top and bottom edges leading to a graver error on the flux density than at the mean radius.

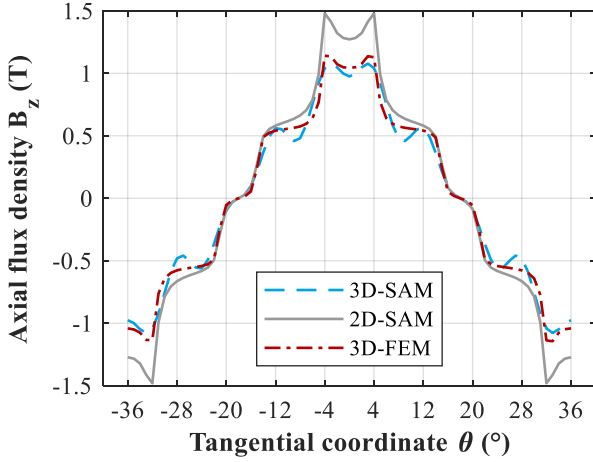


Fig. 6. Axial component of the flux density around the outer radius, in the middle of the air-gap under no-load condition ( $W_b = 1 \text{ mm}$ ,  $r = R_2 - 2 \text{ mm}$ ,  $z = W_a + W_b/2$  and  $\delta = 0$ ).

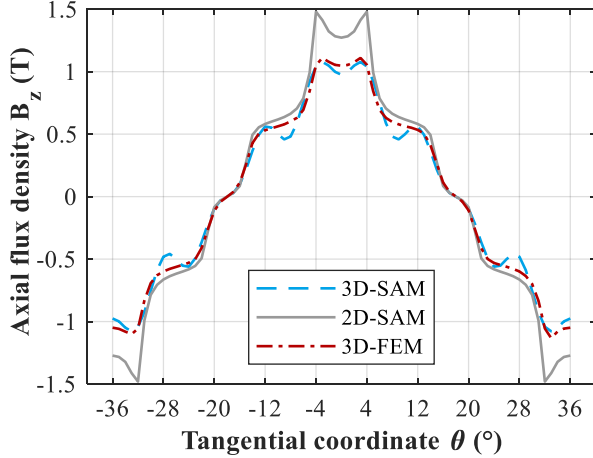


Fig. 7. Axial component of the flux density around the inner radius, in the middle of the air-gap under no-load condition ( $W_b = 1 \text{ mm}$ ,  $r = R_1 + 2 \text{ mm}$ ,  $z = W_a + W_b/2$  and  $\delta = 0$ ).

### B. Torque and axial force

Although the accuracy on the magnetic field distribution remains an important matter, the primary aim of an analytical model is to be precise on the values relevant for the actuator sizing. In the case of our magnetic coupling, the relevant values are the pull-out torque and the maximum axial force.

If we consider only the first space harmonic, the pull-out torque of a reluctance coupling is reached for a torque angle  $\delta = \pi/4p$  corresponding to  $\delta = 9^\circ$  for the coupling of Table I [11]. However, because of the other space harmonics as well as saturation effects, the pull-out torque is actually reached at a higher  $\delta$ . Nevertheless, as will be observed in the next section, the torque value at  $\delta = 9^\circ$  still provides a very precise estimate of the pull-out torque.

Fig. 8 shows the pull-out torque as a function of the air-gap length for the three compared models. For large air-gaps, the pull-out torque is well predicted by the both analytical models. However, for small air-gaps, the 3D-SAM appears to be more accurate than 2D-SAM.

Fig. 9 shows the axial force in no-load condition ( $\delta = 0$ ) as a function of the air-gap length. Similar observations to those

of Fig. 8 can be made as the three models converge for large air-gaps whereas the accuracy of 2D-SAM decreases for small air-gaps compared to 3D-SAM.

Indeed, the small air-gap configurations correspond to saturated cases, therefore, the ability of 3D-SAM to account for the iron saturation provides a significant gain in accuracy for both pull-out torque and axial force.

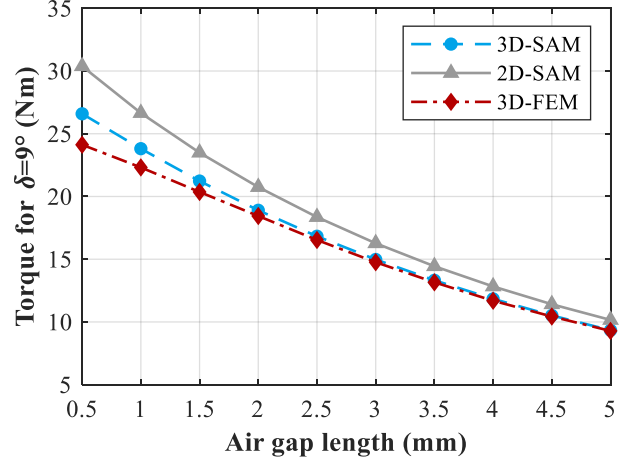


Fig. 8. Torque versus the air-gap length for a torque angle of  $\delta = 9^\circ$ .

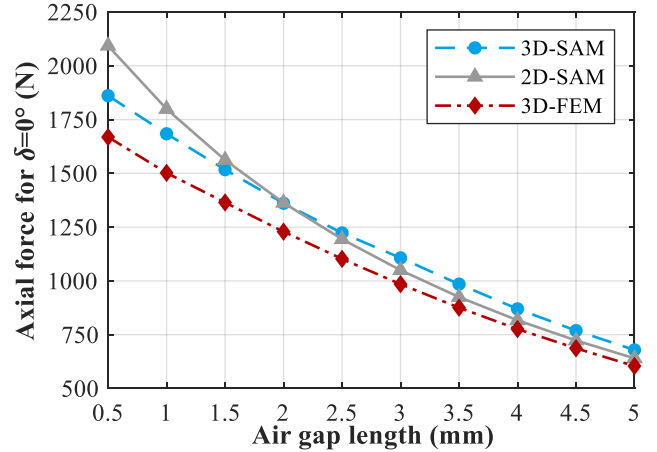


Fig. 9. Axial force versus the air-gap length for a torque angle of  $\delta = 0^\circ$ .

Fig. 10 presents the pull-out torque as a function of the SP opening  $\beta$  for an air-gap length of 1 mm. In [11], this graph highlighted the necessity of considering the magnetic saturation as the 2D-SAM is unable to predict the pull-out torque for very thin SP. In contrast, the 3D-SAM is much closer to the actual behavior but it is still not able to predict the optimal SP opening (i.e.  $\beta = 0.3$ ) for  $N = 10$  harmonics. Therefore, we plotted the results provided by the 3D-SAM for  $N = 15$  harmonics. These additional data show that the accuracy of the 3D-SAM can be further improved by increasing the number of harmonics as the 3D-SAM with  $N = 15$  exhibits an optimal SP opening at  $\beta = 0.25$  whereas the 3D-SAM with  $N = 10$  predicted  $\beta = 0.2$ .

Quite obviously, it is expected that increasing  $N$  will increase the model accuracy. However, this comes at a significant computational cost. Indeed, the 3D-SAM computation time is comprised between 1 and 15 s for  $N = 10$



against 4 and 40 s for  $N = 15$ . The high variability of the computation time is due to the number of iterations required in the saturation algorithm. As a comparison, the 2D-SAM takes less than 50 ms to compute and the 3D-FEM about 3 min.

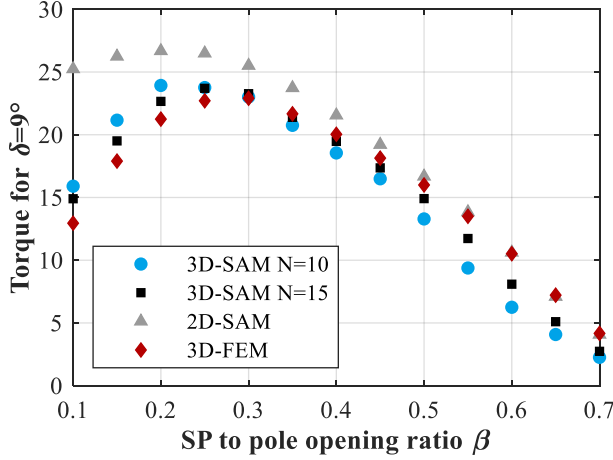


Fig. 10. Torque versus the SP opening for an air-gap length of 1 mm and a torque angle of  $\delta = 9^\circ$ .

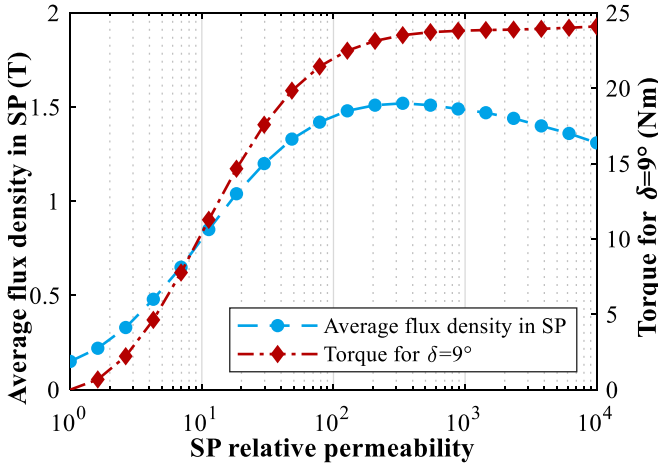


Fig. 11. Influence of the SP permeability on the average flux density in the SP (left-axis) and on the torque (right-axis) obtained with 3D-SAM without the saturation algorithm.

An additional limitation of the 3D-SAM can be observed on Fig. 11. For this figure, we deactivated the saturation algorithm allowing us to plot the average flux density in the SP as a function of the SP imposed relative permeability. Although the average flux density is expected to increase with the permeability, it can be seen that it actually reaches a maximum around  $\mu_r = 350$ . Indeed, since the discontinuity in the non-uniform permeability in region III increases with  $\mu_r$ , the magnetic field values are more difficult to compute in this region leading to inaccuracies. Nonetheless, we also plotted the pull-out torque versus  $\mu_r$  and it appears to be constantly increasing as expected. Moreover, this issue did not alter the convergence of the saturation algorithm and did not seem to affect significantly the accuracy on the important quantities such as torque or axial force.

According to the previous observation, it appears that the 3D-SAM is mainly suited to SP saturated cases. Indeed, in non-saturated cases, Figs 4-6 showed that the 2D-SAM model is

accurate enough and at a much lower computation cost. Additionally, the issue highlighted by Fig. 11 appears in non-saturated cases only.

#### IV. COMPARISON WITH EXPERIMENTAL RESULTS

In order to experimentally validate the proposed model, we used the test bench presented in [11]. The first measurements were performed with an air-gap value of 2.9 mm to validate the model in non-saturated cases.

Fig. 12 shows the experimental setup for the static torque measurement. The torque is measured by suspending weights at the end of a 0.5 m rod connected to the SP rotor shaft whereas the PM rotor was fixed. The torque angle  $\delta$  corresponds to the difference between the angular position of both rotors. The position of a first rotor is blocked at  $0^\circ$  whereas the position of the second rotor is measured using an incremental encoder (resolution of 4096 pulses/revolution).

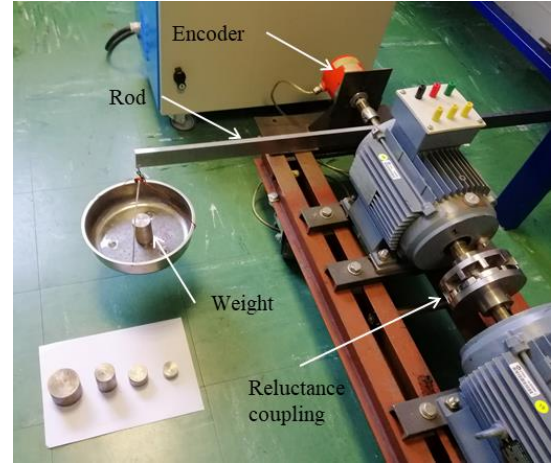


Fig. 12. Picture of the experimental setup for the torque measurement [11].

Fig. 13 shows the experimental setup for the air-gap flux density distribution measurement. A Hall probe is inserted in the air-gap to measure the flux density at different locations. It should be noted that this procedure could not be realized for small air gaps as the Hall probe did not fit between PM and SP.

Fig. 14 shows the axial component of the flux density distribution along the  $\theta$ -direction measured in the middle of the air-gap, at the mean radius under no-load condition ( $\delta = 0$ ) and compared with the three models. For such a large air-gap, the difference between the models and measurements are indistinguishable. Indeed, in this configuration, the SP are not saturated, the curvature and end effects are negligible (measurement at the mean radius), thus the assumptions of all models are valid.

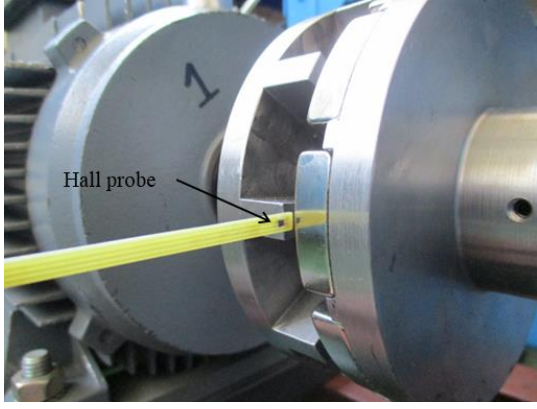


Fig. 13 Picture of the experimental setup for the flux density measurement.

Fig. 15 shows the axial component of the flux density distribution along the  $r$ -direction measured in the middle the air-gap, at the center of the SP and PM under no-load condition ( $\delta = 0$ ), as shown in Fig. 13. Comparisons between the three models are given. In this case, the SP are still not saturated (air-gap of 2.9 mm), but we can observe the end and curvature effects. As was observed on Fig. 12, the 2D-SAM is accurate at the mean radius, but it cannot predict precisely the flux density close to the top and bottom edges of the coupling, as shown in Fig. 15. However, the 3D-SAM, which considers the end effects, is much closer to the measurements. The impact of the curvature effects, neglected by the 3D-SAM, can be observed in both the measurement and 3D-FEM which are unsymmetrical with respect to the mean radius contrary to the 3D-SAM. Nevertheless, the errors produced by this assumption are minor, which confirms the curvature effects are a secondary order phenomenon.

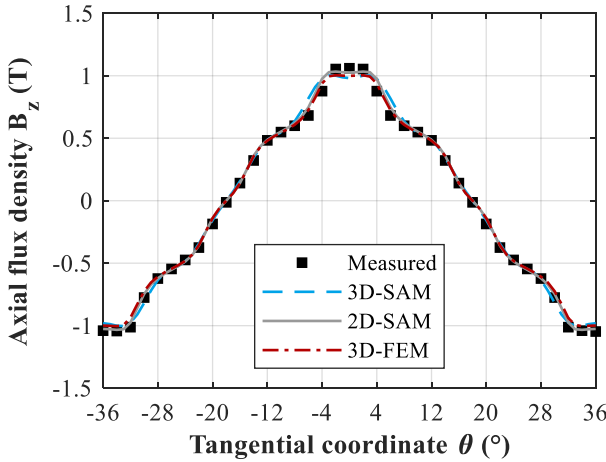


Fig. 14. Axial component of the flux density measured at the mean radius, in the middle of the air-gap under no-load condition ( $W_b = 2.9 \text{ mm}$ ,  $r = R_m$ ,  $z = W_a + W_b/2$  and  $\delta = 0$ ).

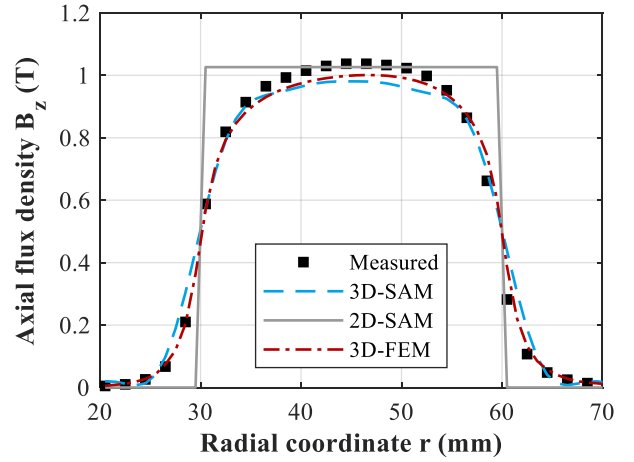


Fig. 15. Axial component of the flux density along the  $r$ -direction in the middle of the air-gap under no-load condition ( $W_b = 2.9 \text{ mm}$ ,  $\theta = 0$ ,  $z = W_a + W_b/2$  and  $\delta = 0$ ).

Fig. 16 shows measured static torque as a function of the torque angle  $\delta$  compared with the three models for an air-gap of 2.9 mm. As for the results of Fig. 8, the results of the three models are close to each other for this air-gap length and the measurements are coherent with the three models. It should be noted that although the 2D-SAM has been judged less accurate than 3D-SAM in the previous section, the error made in non-saturated cases are of the same order as the measurement's errors. Moreover, this result shows the relevancy of the correction factor introduced in the 2D-SAM by [11] which partially account for the end effects in the torque and axial force calculation.

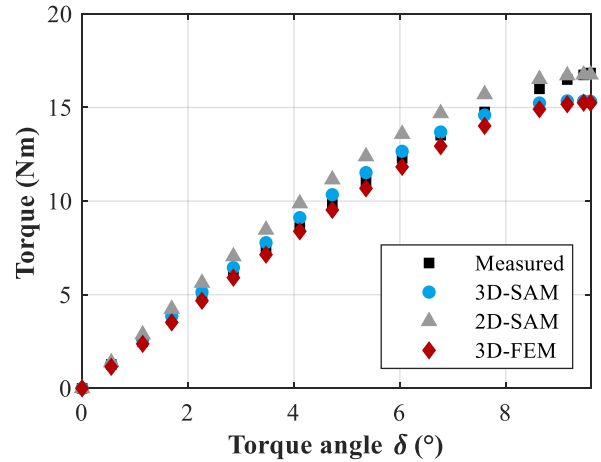


Fig. 16. Measured and calculated torque function of the torque angle  $\delta$  for an average air-gap length of 2.9 mm.

In order to assess the validity of the proposed model in saturated cases, we made an additional test after reducing the air-gap length to 0.73 mm.

Fig. 17 compares the measured static torque as a function of  $\delta$  for the three models. We can observe more dispersed results than the ones given in Fig. 16, highlighting the influence of the SP saturation. As expected, the 2D-SAM is the least accurate as the coupling's SP are saturated. Indeed, the 2D-SAM overestimate the pull-out torque by 17.5 % whereas the 3D-

SAM only overestimate it by 3.5 % which shows the relevancy of the proposed model.

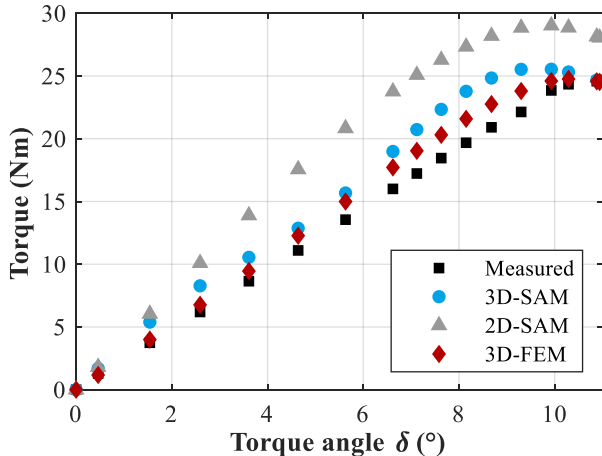


Fig. 17. Measured and calculated torque function of the torque angle  $\delta$  for an average air-gap length of 0.73 mm.

As mentioned earlier it appears on Fig. 17 that the pull-out torque is not obtained at  $\delta = 9^\circ$  but was measured at  $\delta = 10.9^\circ$  whereas the models predicted it around  $\delta = 10^\circ$ . In any case, the torque measured around  $\delta = 9^\circ$  represents about 95 % of the pull-out torque which validates the approximation made in the last section.

It should be noted though, that the angle corresponding to the pull-out torque is rather difficult to measure especially with the proposed method. Indeed, close to the pull-out torque, the coupling is very sensitive to small imbalances because the difference between the torque at  $\delta = 9^\circ$  and  $\delta = 10.9^\circ$  is very small. Moreover, small air-gaps values are difficult to precisely set because of the large axial forces and since the coupling becomes more vulnerable to misalignments. All these reasons lead to measurement errors which explain the differences between the measurements and 3D-FEM.

## V. CONCLUSION

In this article, we proposed a 3-D semi-analytical model (3D-SAM) of a reluctance coupling accounting for the global magnetic saturation in the salient-pole. The goal of this model is to deal with the situations outside of the validity area of a previously developed 2-D semi-analytical model (2D-SAM) [11]. The new model is based on the Cauchy's product and the matrix form which allows to implement subdomains with a spatially variable magnetic permeability in two directions. By using this technique, we managed to model the geometry with only three subdomains and implement an iterative algorithm to account for the non-linear magnetic behavior of the SP.

The 3D-SAM and the previously developed 2D-SAM have been compared with 3D-FEM as well as experimental measurements on a reluctance magnetic coupling test bench for wide and short air-gaps.

In the non-saturated cases, which correspond to the validity area of the 2D-SAM, all the models appeared to be accurate for the torque and axial force calculation. However, for the flux

density distribution, the 2D-SAM is precise only at the mean radius since the end effects are only considered for the torque and axial force calculation through a correction factor whereas the 3D-SAM accounts for the end effects completely. Moreover, neglecting the curvature effects has proved to be a relevant and particularly useful assumption.

Furthermore, the 3D-SAM managed to overcome the limitations of the 2D-SAM in situations where the SP are saturated, notably by accurately predicting the pull-out torque, for small air-gaps or for small SP opening, which is the most important output parameter of a magnetic coupling.

However, the accuracy improvements made by the 3D-SAM comes at the expense of the computational cost and complexity of implementation compared to the 2D-SAM. Therefore, although both models are suitable for optimization and design processes as they are still faster than the FEM, the 2D-SAM appear as the appropriate option to design couplings expected to be used with non-saturated SP. Nonetheless, optimal geometries of magnetic actuators are frequently in saturated situations. Thus, the 3D-SAM remain a more relevant option in the general case.

Additionally, the model proposed in this paper and the one presented in [11] are two modelling examples, the first one with few assumptions and the second one requiring more assumptions but providing a minimal computational cost. One can note that the method presented here can be applied with more or less assumptions, depending on the need, to improve the computation time. For instance, if the saturation is not significant for the intended application, the saturation algorithm can be removed which would drastically reduce the computation time. Alternatively, it is possible to apply the model in 2-D with the correction factor while keeping the iterative algorithm in order to reduce the overall number of harmonics.

Finally, the proposed model can be adapted to other kind of axial-flux actuators comprising salient poles, such as the calculation of the torque ripple in axial-flux PM machines, under some slight modifications.

## REFERENCES

- [1] J. F. Charpentier, N. Fadli, and J. Jennane, "Study of ironless permanent magnet devices being both a coupling and an axial bearing for naval propulsion," *IEEE Transactions on Magnetics*, vol. 39, no. 5, pp. 3235–3237, Sep. 2003, doi: 10.1109/TMAG.2003.816732.
- [2] J. Fontchastagner, Y. Lefèvre, and F. Messine, "Some Co-Axial Magnetic Couplings Designed Using an Analytical Model and an Exact Global Optimization Code," *IEEE Transactions on Magnetics*, vol. 45, no. 3, pp. 1458–1461, Mar. 2009, doi: 10.1109/TMAG.2009.2012678.
- [3] Y. Li *et al.*, "Analytical Analysis of an Adjustable-Speed Permanent Magnet Eddy-Current Coupling With a Non-Rotary Mechanical Flux Adjuster," *IEEE Transactions on Magnetics*, vol. 55, no. 6, pp. 1–5, Jun. 2019, doi: 10.1109/TMAG.2019.2893458.
- [4] J. Wang, H. Lin, S. Fang, and Y. Huang, "A General Analytical Model of Permanent Magnet Eddy Current Couplings," *IEEE Transactions on Magnetics*, vol. 50, no. 1, pp. 1–9, Jan. 2014, doi: 10.1109/TMAG.2013.2279073.
- [5] K. Li, J. Z. Bird, and V. M. Acharya, "Ideal Radial Permanent Magnet Coupling Torque Density Analysis," *IEEE Transactions on Magnetics*, vol. 53, no. 6, pp. 1–4, Jun. 2017, doi: 10.1109/TMAG.2017.2668139.
- [6] T. Lubin, S. Mezani, and A. Rezzoug, "Simple Analytical Expressions for the Force and Torque of Axial Magnetic Couplings," *IEEE Transactions on*

*Energy Conversion*, vol. 27, no. 2, pp. 536–546, Jun. 2012, doi: 10.1109/TEC.2012.2183372.

[7] M. H. Nagrial, “Analysis and performance of variable reluctance (VR) torque coupler,” in *Proceedings IEEE Conference on Industrial Automation and Control Emerging Technology Applications*, May 1995, pp. 136–139, doi: 10.1109/IACET.1995.527552.

[8] B. Dolisy, S. Mezani, T. Lubin, and J. L  v  que, “A New Analytical Torque Formula for Axial Field Permanent Magnets Coupling,” *IEEE Transactions on Energy Conversion*, vol. 30, no. 3, pp. 892–899, Sep. 2015, doi: 10.1109/TEC.2015.2424159.

[9] T. Lubin and A. Rezzoug, “3-D Analytical Model for Axial-Flux Eddy-Current Couplings and Brakes Under Steady-State Conditions,” *IEEE Transactions on Magnetics*, vol. 51, no. 10, pp. 1–12, Oct. 2015, doi: 10.1109/TMAG.2015.2455955.

[10] T. Lubin and A. Rezzoug, “Improved 3-D Analytical Model for Axial-Flux Eddy-Current Couplings With Curvature Effects,” *IEEE Transactions on Magnetics*, vol. 53, no. 9, pp. 1–9, Sep. 2017, doi: 10.1109/TMAG.2017.2714628.

[11] T. Lubin, A. A. Vahaj, and A. Rahideh, “Design optimisation of an axial-flux reluctance magnetic coupling based on a two-dimensional semi-analytical model,” *IET Electric Power Applications*, vol. 14, no. 5, pp. 901–910, 2020, doi: <https://doi.org/10.1049/iet-epa.2019.0746>.

[12] F. Dubas and K. Boughrara, “New Scientific Contribution on the 2-D Subdomain Technique in Cartesian Coordinates: Taking into Account of Iron Parts,” *Mathematical and Computational Applications*, vol. 22, no. 1, Art. no. 1, Mar. 2017, doi: 10.3390/mca22010017.

[13] L. Roubache, K. Boughrara, F. Dubas, and R. Ibtiouen, “New Subdomain Technique for Electromagnetic Performances Calculation in Radial-Flux Electrical Machines Considering Finite Soft-Magnetic Material Permeability,” *IEEE Transactions on Magnetics*, vol. 54, no. 4, pp. 1–15, Apr. 2018, doi: 10.1109/TMAG.2017.2785254.

[14] R. L. J. Sprangers, J. J. H. Paulides, B. L. J. Gysen, and E. A. Lomonova, “Magnetic Saturation in Semi-Analytical Harmonic Modeling for Electric Machine Analysis,” *IEEE Transactions on Magnetics*, vol. 52, no. 2, pp. 1–10, Feb. 2016, doi: 10.1109/TMAG.2015.2480708.

[15] Z. Djelloul-Khedda, K. Boughrara, F. Dubas, A. Kechroud, and B. Souleyman, “Semi-Analytical Magnetic Field Predicting in Many Structures of Permanent-Magnet Synchronous Machines Considering the Iron Permeability,” *IEEE Transactions on Magnetics*, vol. 54, no. 7, pp. 1–21, Jul. 2018, doi: 10.1109/TMAG.2018.2824278.

[16] H. S. Zhang, Z. X. Deng, M. L. Yang, Y. Zhang, J. Y. Tuo, and J. Xu, “Analytical Prediction of Halbach Array Permanent Magnet Machines Considering Finite Tooth Permeability,” *IEEE Transactions on Magnetics*, vol. 56, no. 6, pp. 1–10, Jun. 2020, doi: 10.1109/TMAG.2020.2982844.

[17] Z. Djelloul-Khedda, K. Boughrara, F. Dubas, and R. Ibtiouen, “Nonlinear Analytical Prediction of Magnetic Field and Electromagnetic Performances in Switched Reluctance Machines,” *IEEE Transactions on Magnetics*, vol. 53, no. 7, pp. 1–11, Jul. 2017, doi: 10.1109/TMAG.2017.2679686.

[18] H. Zhao, C. Liu, Z. Song, and J. Yu, “Analytical Modeling and Comparison of Two Consequent-Pole Magnetic-Geared Machines for Hybrid Electric Vehicles,” *Energies*, vol. 12, no. 10, Art. no. 10, Jan. 2019, doi: 10.3390/en12101888.

[19] R. Dorget, T. Lubin, S. Ayat, and J. L  v  que, “3-D Semi-analytical model of a superconducting axial flux modulation machine,” *IEEE Transactions on Magnetics*, pp. 1–1, 2021, doi: 10.1109/TMAG.2021.3108632.

[20] Z. Luo, S. Nie, M. Pathmanathan, W. Han, and P. W. Lehn, “3-D Analytical Model of Bipolar Coils with Multiple Finite Magnetic Shields for Wireless Electric Vehicle Charging Systems,” *IEEE Transactions on Industrial Electronics*, pp. 1–1, 2021, doi: 10.1109/TIE.2021.3109519.

[21] L. Li, “Use of Fourier series in the analysis of discontinuous periodic structures,” *J. Opt. Soc. Am. A, JOSAA*, vol. 13, no. 9, pp. 1870–1876, Sep. 1996, doi: 10.1364/JOSAA.13.001870.



**R  mi Dorget** was born in Saint-Maur-des-Foss  s, France in 1996. He received the M.S. degree in electrical engineering from the University of Lorraine, Nancy, France, in 2019. He is currently PhD student with Safran tech in the “Electrical and Electronic Systems Research group” and the University of Lorraine in the “Groupe de Recherche en Energie Electrique de Nancy, GREEN”. His research topics are the design, the construction and the tests of superconducting electrical machines.



**Thierry Lubin** received the M.S. degree in electrical engineering from the University Pierre et Marie Curie, Paris, France, in 1994, and the Ph.D. degree from the University of Lorraine, Nancy, France, in 2003. He is currently an Associate Professor of Electrical Engineering with the Faculty of Sciences and Technology, University of Lorraine, Nancy, where his research works are undertaken in the “Groupe de Recherche en Energie Electrique de Nancy, GREEN”. His research interests include analytical modeling of electrical machines, contactless torque transmissions by magnetic gears and couplers, and the use of superconductors in electromechanical devices.